ISSN: 0256-307X

中国物理快报
Chinese Physics Letters

Volume 27 Number 1 January 2010

A Series Journal of the Chinese Physical Society
Distributed by IOP Publishing

Online: http://www.iop.org/journals/cpl
http://cpl.iphy.ac.cn

CHINESE PHYSICAL SOCIETY

CHIN. PHYS. LETT. Vol. 27, No. 1 (2010) 019601

Ion Velocity Distributions in a Non-Stationary Perpendicular Shock *

YANG Zhong-Wei(杨忠炜)[1,2], LUQuan-Ming(陆全明)[1,2**], WANG Shui(王水)[1]

[1]*CAS Key Laboratory of Basic Plasma Physics, School of Earth and Space Sciences, University of Science and Technology of China, Hefei 230026*

[2]*State Key Laboratory of Space Weather, Chinese Academy of Sciences, Beijing 100190*

(Received 24 August 2009)

Previous particle-in-cell simulations have evidenced that supercritical, quasi-perpendicular shocks are non-stationary. By separating the incident ions into reflected (R) and directly transmitted (DT) parts, we investigate the ion distributions in a non-stationary perpendicular shock. The upstream ion distributions have two parts corresponding to the R and incident ions respectively, while the R ions have higher energy. The downstream ions have a core-ring distribution. The core and ring parts correspond to the DT and R ions, respectively. The ion distributions depend largely on the non-stationary shock structure. The percentage of the reflected ions cyclically varies in time with a period equal to the shock self-reformation cycle, and the number of the R ions increases with the steepness of the shock ramp.

PACS: 96.50.Fm, 94.05.Pt, 96.50.Ry

Collisionless shocks are of great interest since in the shock transition the bulk energy of the plasma is converted irreversibly into thermal energy.[1,2] According to θ_{nB} (the angle between the shock normal and upstream magnetic field), shocks can be separated into two groups: quasi-parallel shocks ($\theta_{nB} < 45°$) and quasi-perpendicular shocks ($\theta_{nB} > 45°$). Many theoretical and numerical studies have indicated that the dissipation in subcritical (low Mach number), quasi-perpendicular shocks is provided by resistive heating. This heating is associated with the strong electron currents required to produce the steep gradients in the magnetic field across the shock front.[3] However, in supercritical (high Mach number), quasi-perpendicular shocks, an additional dissipation mechanism is needed to satisfy the Rankine–Hugoniot conditions across the shock, since dissipation provided by resistivity is not sufficient. Ion reflection is considered to be the dominant dissipation mechanism in supercritical, quasi-perpendicular shocks.[4]

Ion reflection in supercritical, quasi-perpendicular shocks has been confirmed by spacecraft observations[5] and hybrid simulations.[6] The reflected ions gyrate back to the shock immediately, and then across the shock directly. During this process, the reflected ions gain a larger kinetic perpendicular temperature than the parallel one, and excite ion cyclotron waves downstream of the shock.[7,8] In this way, ion reflection provides the dominant dissipation at supercritical, quasi-perpendicular shocks. Whether a particle becomes reflected depends on its energy in the upstream frame and its gyro-phase as it encounters the shock.[9] Furthermore, effects of the angle θ_{nB}, the radio of the ion thermal velocity to the flow velocity upstream, and the cross-shock potential on distributions of reflected ions in a stationary quasi-perpendicular shock are presented by Gedalin *et al.*[10] They concluded that a typical distribution of reflected ions exhibits a bimodal pitch angle distribution in the upstream. However, the shock profiles they used were not obtained self-consistently.

Particle-in-cell simulations clearly evidenced that supercritical, quasi-perpendicular shocks are non-stationary and suffer a self-reformation on the gyro scale of the incident ions due to the accumulation of reflected ions (foot formation).[11,12] More precisely, the cyclic period of this process is of the order of ion gyro-period calculated from the average magnetic field measured in the middle of the ramp as measured by Lembge and Savoini.[13] Recently, the shock front reformation phenomenon is also confirmed in hybrid simulations with a smaller grid size[14] and Cluster spacecraft observations.[15] In this letter, a particle-in-cell (PIC) code is used to investigate the ion distributions upstream and downstream in a supercritical, perpendicular shock.

In this study, self-consistent perpendicular shock profiles are obtained from a 1-D PIC simulation. The initial and boundary conditions are identical to those already described in detail by Lembège and Savoini;[13] the shock is initiated by a magnetic piston (utilized current pulse). Briefly, the shock geometry is defined in the upstream frame: the shock propagates along the x axis and a static magnetic field is applied along the z axis. All dimensionless quantities are indicated by a tilde and are normalized as follows. The spatial coordinate is $\tilde{x} = x/\Delta$; velocity $\tilde{v} = v/\omega_{pe}\Delta$; time $\tilde{t} = \omega_{pe}t$, electric field $\tilde{E} = eE/m_e\omega_{pe}^2\Delta$; magnetic field $\tilde{B} = eB/m_e\omega_{pe}^2\Delta$. The parameters Δ, ω_{pe}, m_e and e are, respectively, the numerical grid size, the electron plasma frequency, the electron mass and the electric charge. All basic parameters are identical to those employed by Hada *et al.*,[11] i.e. plasma box size length $L_x = 4096$, velocity of light $\tilde{c} = 3$,

*Supported by the National Natural Science Foundation of China under Grant Nos 40874075, 40725013 and 4094093, and the Knowledge Innovation Project of Chinese Academy of Sciences under Grant No KJCX2-YW-N28.

**Email: qmlu@ustc.edu.cn

and mass ratio $m_i/m_e = 84$. Initially, the particle density is $n_e = n_i = 50$ at each grid point. The electron/ion temperature ratio $T_e/T_i = 1.58$ is chosen. The ambient magnetic field is $|\tilde{B}_0| = 1.5$. The shock front is propagating in a supercritical regime with the average Mach number about ($M_A = 5.24$), where $M_A = \tilde{V}_{\rm shock}/\tilde{V}_A$ is determined in the upstream frame; the Alfven velocity $\tilde{V}_A$ equals to 0.16 and the shock propagating speed $\tilde{V}_{\rm shock}$ is the moving speed of the shock ramp. The shock ramp is defined as the position with peak $\partial\tilde{B}_z^2/\partial x$. For these initial conditions, the plasma parameters are summarized in Table 1 for both electrons and ions. The Larmor gyro radius in the table is calculated based on thermal velocity.

Table 1. Upstream plasma parameters defined for PIC simulations.

		Electrons	Ions
Thermal velocity	$\tilde{V}_{thx,y,z}$	0.2	0.017
Debye length	$\tilde{\lambda}_D$	0.2	0.16
Larmor gyro radius	$\tilde{\rho}_c$	0.4	2.91
Inertia length	$\tilde{c}/\tilde{\omega}_p$	3.0	27.5
Gyro frequency	$\tilde{\omega}_c$	0.5	0.006
Plasma frequency	$\tilde{\omega}_p$	1.0	0.11
Gyro period	$\tilde{\tau}_c$	12.55	1055.46
Plasma beta	$\tilde{\beta}$	0.0355	0.0225

Figure 1 shows the time evolution of the magnetic field $\tilde{B}_z$ from $\tilde{t} = 1200$ to 2064. The shock is propagating from the left to the right. At about $\tilde{t} = 1200$, the shock front is at about $\tilde{X} = 5070$. Later at about $\tilde{t} = 1350$, the relatively high percentage of reflected ions has accumulated in the foot so that the foot amplitude becomes sufficiently large and comparable to that of the "old" ramp. Then, a "new" shock ramp builds up and starts reflecting new incoming ions. The "new" shock front is well formed around $\tilde{X} = 5320$ at about $\tilde{t} = 1490$. Simultaneously, the "old" shock front becomes weaker and weaker, and is located downstream of the "new" front. The shock front is characterized by a self-reformation with a cyclic period about $288\omega_{pe}^{-1} \approx 1.73\Omega_{ci}^{-1}$. It is found that oblique shock waves can possess a linear whistler precursor. In a supercritical quasi-perpendicular shock, the ramp region can be treated as a nonlinear large-amplitude whistler wave. Because the dispersion cannot prevent steepening of the shock front due to nonlinear effects, the stationary nonlinear whistler wave train cannot exist anymore within the shock front. Therefore, the shock wave becomes nonstationary, and a self-reformation occurs.[16]

We investigate ion distributions in detail in this non-stationary perpendicular shock. The ion distributions at three different regions R-1, R-2 and R-3, which represent upstream region, immediate downstream region and far downstream region, respectively, are studied. The width of each region is 100, and the boundary between R-1 and R-2 is the ramp. We investigate the ion distributions in two regimes: one is a fixed shock regime, where three typical shock profiles are selected, and we study the ion distributions in such fixed profiles. The other is time-evolving shock regime, where the shock is reforming, and the ion distributions are investigated in such a non-stationary shock. In both regimes, we separate the upstream ions into two groups: the reflected (R) ions and directly transmitted (DT) ions. The reflected ions have the following characteristics: after being reflected, (1) their velocity in the x direction $\tilde{v}_{ix}$ is larger than the shock propagating speed $\tilde{V}_{\rm shock}$, and (2) they are located upstream of the ramp $\tilde{x}_i > \tilde{x}_{\rm ramp}$. The separation technology is identical to those already successfully used by Yang *et al.*[17]

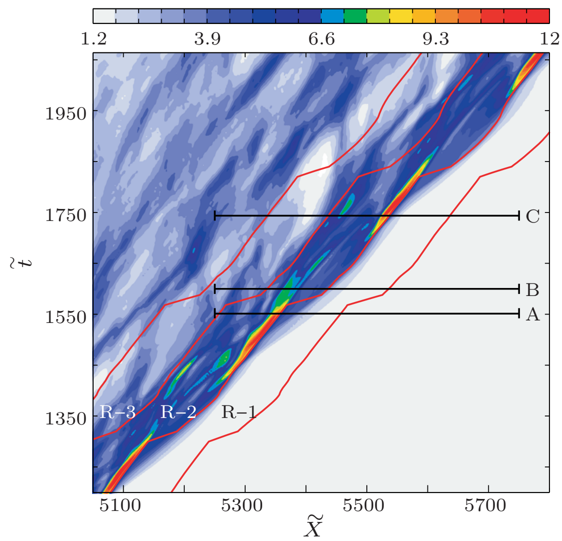

Fig. 1. The time evolution of $\tilde{B}_z$. Labels A, B, C indicate the shock profiles. The four red curves indicate the moving observation windows, which are denominated as R-1, R-2 and R-3 from the right to the left.

In the fixed shock regime, three typical shock profiles (A, B and C) are selected from one self-reformation cycle (from $\tilde{t} = 1456$ to 1744), as shown in Fig. 2. Profile A, B and C represent the snapshots of $\tilde{B}_z$, $\tilde{E}_y$ and $\tilde{E}_x$ at $\tilde{t} = 1552$, 1600 and 1744, respectively. In profile A, the shock front includes a ramp and a foot in front of the ramp, and the position of the ramp is denoted by O (old ramp). In profile B, the amplitude of the ramp O has decreased. Simultaneously, the foot amplitude increases and reaches a value at least equal to 50% of that of the ramp O and becomes a new ramp N. In profile C, the amplitude of the new ramp has already overcome the old one. For profiles B and C, the reference ramp used herein is the main new ramp (denoted by N), which has larger $\tilde{E}_x$ than the old ramp (denoted by O). The reference ramps of profiles A, B and C are respectively at $\tilde{X} = 5359$, 5436, and 5537, and their corresponding "instantaneous" propagating speeds along the x direction are $5.47\tilde{V}_A$, $6.25\tilde{V}_A$ and $3.91\tilde{V}_A$. Their corresponding shock front widths are about $\tilde{\delta} = 70$, 98, and 42. The width of the shock front is measured from the beginning of the foot to the maximum point of the magnetic overshoot,[18] and the start of the foot is defined operationally as the location

where the magnetic field has increased by 6.67% over its upstream value.[9] The ion distributions are studied with a test particle simulation. The test particle simulations are carried out as follows: 126000 test particle ions drawn from a Maxwellian distribution with thermal speed $\tilde{V}_{thx,y,z} = 0.017$ are distributed evenly in the far upstream region $100 < \tilde{x}_i - \tilde{x}_{\rm ramp} < 2620$, where $\tilde{x}_i$ is the initial position of ion i, and $\tilde{x}_{\rm ramp}$ is the initial position of the shock ramp. The width of the upstream region filled with test particles is sufficiently large (approximately $92\tilde{c}/\tilde{\omega}_{pi}$, where $\tilde{\omega}_{pi}$ is the ion plasma frequency). Test particles cease to be followed when swept out of the computational boundaries.

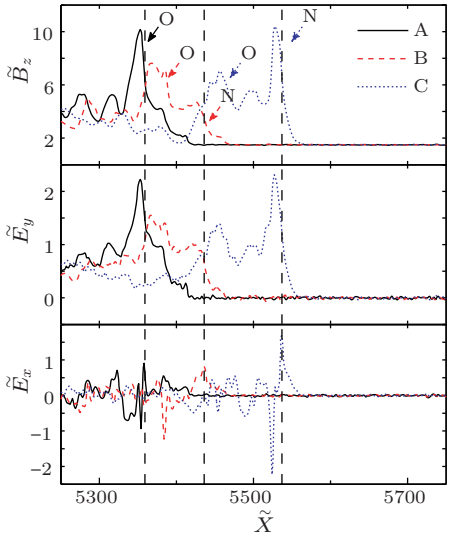

Fig. 2. Plots of the shock profiles at three typical times. "O" and "N" denote positions of the old and new ramps during one reforming cycle, respectively (line A: $\tilde{t} = 1552$, line B: $\tilde{t} = 1600$, line C: $\tilde{t} = 1744$). The reference ramp location is marked by the dashed line for each profile.

Figure 3 shows the ion distributions from upstream to downstream (i.e. from R-1 to R-3) at shock profile A (panel a), B (panel b), and C (panel c). Correspondingly, sketch of $\tilde{B}_z$ of each profile are shown for reference (blue curves). At profile A, the black dots in R-1 indicate the incident ions which have not yet reached the ramp, and the red dots indicate the reflected ions. In R-2, the black dots stand for the DT ions, while the red dots stand for the R ions which return to the shock again and succeed to transmit downstream. In R-3, there is a small change in the distribution of R and DT ions due to the electrostatic drift. The energy of the R ions is always larger than that of the DT ones. At profile B, the amplitude of overshoot decreases and the shock front becomes very broad. The foot is growing up but is not sufficiently high, and there is no R ion in R-1. In R-2, the DT ions form a ring distribution due to the reflection of the old ramp. In R-3, the ion distribution changes due to the electrostatic drift.

At profile C, a steepened new ramp has completely built up and the overshoot reaches the maximum amplitude. In R-1, all of the ions are reflected to upstream (marked by I). A fraction of them are reflected twice (marked by II), and accelerated to higher energy. In R-2, a thick ring distribution is formed by those R ions after they return to the shock and transmit to downstream. In the region, the incident ions (black dots) will return to upstream, and then transmit to downstream again. In R-3, the distribution of the R ions still has a thick ring. Obviously, the ion distributions can be clearly explained by the results in fixed shock regime described above.

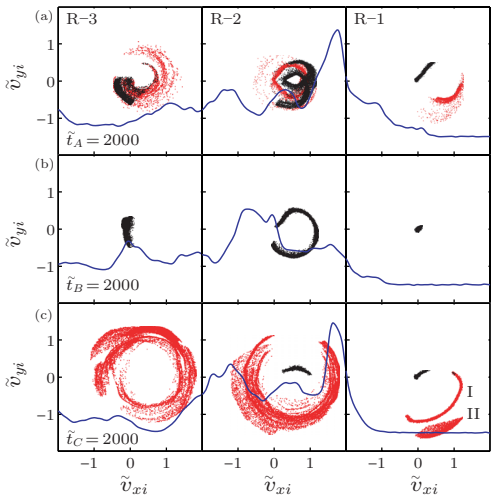

Fig. 3. The ion distributions at shock profile A (a), B (b) and C (c). The red dots represent the reflected ions, and the others ions are marked in black. Left, middle and right column exhibit the ions observed in R-3, R-2 and R-1 observation windows respectively. Corresponding, sketch of the $\tilde{B}_z$ of each profile are shown for reference (blue curves). Here $\tilde{t}_A$, $\tilde{t}_B$ and $\tilde{t}_C$ are measured from the time when profile A, B and C are chosen, respectively. I and II indicate the R ions, which are reflected once and twice.

In the time-evolving shock regime, we investigate ion distribution when the shock is non-stationary as shown in Fig. 1. 126000 particle ions drawn from a Maxwellian distribution with thermal speed $\tilde{V}_{thx,y,z} = 0.017$ are distributed evenly in the far upstream region $100 < \tilde{x}_i - \tilde{x}_{\rm ramp} < 2620$ at a chosen time $\tilde{t} = 628$. In the simulation, the width of the upstream region filled with particles is sufficiently large, and it takes about 5 shock reformation cycles to advect those particles through the shock.

Figure 4 shows a series of snapshots of ion distributions from upstream to downstream (i.e. from R-1 to R-3) at different times within one cycle of shock front self-reformation. Correspondingly, the sketch of the $\tilde{B}_z$ are shown for reference (blue curves). Firstly, we concentrate on the ion distributions in R-1 from panel (a) to (f). During the time $\tilde{t} = 1492$–1524, the shape of shock profile are evolving from type C (similar to profile C) to type A (similar to profile A). A fraction of incident ions are reflected (marked by I). At $\tilde{t} = 1524$, some of the R ions are reflected twice, and form a "S" shape in velocity space. Later on ($\tilde{t} = 1580$

and 1660), the shock profile is of type B (similar to profile B). The number of R ions become less and less because the shock front is too broad to reflect many incident ions. At $\tilde{t} = 1712$, a new ramp of the shock increases and begins to reflect the incident ions again. Therefore there are two groups of R ions in R-1 at this moment: R ions reflected by the old ramp (marked by I), and R ions reflected by the new ramp (marked by II). At $\tilde{t} = 1748$, the new shock front is well formed. The shape of shock profile is of type C (similar to profile C) again. Large numbers of R ions appear in the R-1 again. Obviously, the R ions upstream of the non-stationary shock are intermittent because the shock front is reforming periodically. Then, we focus on the ion distributions in R-2 from panel (a) to (f). From $\tilde{t} = 1580$ to 1748, the R and DT ions are captured by the decreased old ramp and the increased new ramp. During this time, the R ions become more diffuse and gradually form a ring distribution. Finally, the ions in R-3 have a ring-core distribution. The ring is formed by the R ions, while the core is formed by the DT ions.

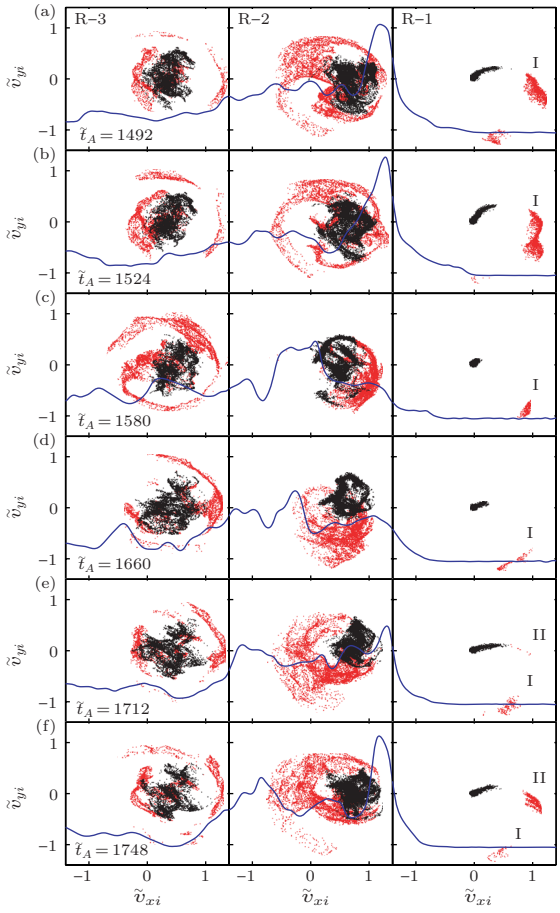

Fig. 4. Snapshots of the ion distributions at different moment within a shock front reformation cycle (a–f). The red dots represent the reflected ions, and the others ions are marked in black. Left, middle and right column exhibit the ions observed in R-3, R-2 and R-1 observation windows respectively. Correspondingly, sketch of the $\tilde{B}_z$ of each profile are shown for reference (blue curves). I and II indicate the R ions, which are reflected by the old and new ramps, respectively.

Reflected ions are an important signature of supercritical, quasi-perpendicular shocks. In this Letter, we investigate the effects of shock front non-stationarity on ion distributions upstream and downstream. We have the following conclusions: Our calculations clearly show that the non-stationary shock front significantly affects the ion distributions upstream. The shock reformation leads to a periodic response of ion reflection. The number of reflected ions increases when the shock front is steep and narrow, and vice versa. Moreover, some of the incident ions are reflected twice when the shock ramp is steep. In the downstream, ions has a ring-core distribution. The ring is formed by the R ions, where the core is formed by the DT ions. Such a ring distribution may be unstable to ion cyclotron waves propagating along the background magnetic field. This effect need to be resolved in a two-dimensional simulation, and is beyond the scope of this letter. The bulk velocities of R and DT ions are nearly the same, and the energy of the R ions is higher than that of the DT ions.

The above conclusions imply that a non-stationary shock front should lead to temporal variations in reflected ions of a quasi-perpendicular shock, and may influence the dissipation of the shock. For example, in the immediate downstream, some of the reflected ions may be captured by the decreased old ramp and the increased new ramp of the shock front and stay for a long time, which may lead to an additional dissipation in the supercritical, quasi-perpendicular shocks.

We thank Dr. Bertrand Lembge for the useful discussions.

References

[1] Lembge B et al 2004 *Space Sci. Rev.* **110** 161
[2] Burgess D et al 2005 *Space Sci. Rev.* **118** 205
[3] Biskamp D 1973 *Nucl. Fusion* **13** 719
[4] Lembge B and Dawson J M 1987 *Phys. Fluids* **30** 1767
[5] Fuselier S A et al 1994 *J. Geophys. Res.* **99** 11539
[6] Lipatov A S and Zank G P 1999 *Phys. Rev. Lett.* **82** 3609
[7] Lu Q M, Wang D Y, and Wang S 2005 *J. Geophys. Res.* **110** A03223 doi: 10.1029/2004JA010739
[8] Lu Q M and Wang S 2006 *J. Geophys. Res.* **111** A05204
[9] Burgess D, Wilkinson W P, and Schwartz S J 1989 *J. Geophys. Res.* **94** 8783
[10] Gedalin M et al 2008 *J. Geophys. Res.* **113** A05101
[11] Hada T, Oonishi M, Lembge B et al 2003 *J. Geophys. Res.* **108** 1233 doi:10.1029/2002JA009339
[12] Scholer M and Matsukiyo S 2004 *Ann. Geophys.* **22** 2345
[13] Lembge B and Savoini P 1992 *Phys. Fluids* B **4** 3533
[14] Hellinger P et al 2002 *Geophys. Res. Lett.* **29** 2234
[15] Lobzin V V et al 2007 *Geophys. Res. Lett.* **34** L05107
[16] Krasnoselskikh et al 2002 *Phys. Plasmas* **9** 1192
[17] Yang Z W et al 2009 *J. Geophys. Res.* **114** A03111
[18] Shimada N and Hoshino M 2005 *J. Geophys. Res.* **110** A02105

Chinese Physics Letters

Volume 27 Number 1 2010

GENERAL

010201 New Solitary Solutions of (2+1)-Dimensional Variable Coefficient Nonlinear Schrödinger Equation with an External Potential
SONG Zhao-Hui, DING Qi, MEI Jian-Qin, ZHANG Hong-Qing

010202 Lie Symmetries, Perturbation to Symmetries and Adiabatic Invariants of a Generalized Birkhoff System
LI Yan-Min

010301 Robust Quantum Computation with Superconducting Charge Qubits via Coherent Pulses
FENG Zhi-Bo, YAN Run-Ying

010302 Criterion for Genuine Multipartite Entanglement Quantum Channels
JIANG Nian-Quan, WANG Yu-Jian

010303 Generators for Symmetric Universal Quantum Cloning Machines
JIANG Ming-Ming, YU Si-Xia

010304 Validity of Lamb–Dicke Approximations in Ion-Trap Systems
LAN Hai-Jiang, ZHANG Miao, WEI Lian-Fu

010305 Holographic Laser as a Source of Continuous Variable Entanglement
YANG Bin, LU Xin-You, WU Meng-Xi

010306 Analytical Solutions to the Klein–Gordon Equation with Position-Dependent Mass for q-Parameter Pöschl–Teller Potential
Altuğ Arda, Ramazan Sever, Cevdet Tezcan

010307 Schemes for Teleportation of an Unknown Single-Qubit Quantum State by Using an Arbitrary High-Dimensional Entangled State
ZHAN You-Bang, ZHANG Qun-Yong, WANG Yu-Wu, MA Peng-Cheng

010308 Quantum Immune Clonal Selection Algorithm for Multi-objective 0/1 Knapsack Problems
SHANG Rong-Hua, JIAO Li-Cheng, LI Yang-Yang, WU Jian-She

010309 Phase-Dependent Effects in Stern–Gerlach Experiments
XU Xu, ZHOU Xiao-Ji

010401 Equation of State in the $\sigma-\omega-\rho$ Model Supported by the Observational Data of 4U 1608-52 Neutron Star
WEN De-Hua

010501 Deterministic Characterization of Intrinsic Noise in Chemical Reactions
YAN Long, WANG Hong-Li, OUYANG Qi

010502 Dynamical Effect of Calcium Pump on Cytosolic Calcium Bursting Oscillations with IP_3 Degradation
MENG Pan, LU Qi-Shao

010503 A Passivity Based Synchronization for Chaotic Behavior in Nonlinear Bloch Equations
Choon Ki Ahn

010504 Cytoplasmic Ca^{2+} Dynamics under the Interplay between the Different IP_3R Gating Models and the Plasma Membrane Ca^{2+} Influx
CHEN Xiao-Fang, LI Cong-Xin, WANG Peng-Ye, WANG Wei-Chi

010701 Modulated Terahertz Transmission through Sub-Wavelength Cu Grating by Liquid Water
CHEN Hua, WU Xiu-Mei, YANG Wen-Xing

THE PHYSICS OF ELEMENTARY PARTICLES AND FIELDS

011101 Boson Nebulae Charge
Ciprian Dariescu, Marina-Aura Dariescu

(Continued on inside back cover)

011201 Non-Strange Baryon Spectra and Confinement in the Constituent Quark Model
LI Quan, PANG Hou-Rong, PING Jia-Lun

011202 Heavy Charged Leptons from Type-III Seesaw and Pair Production of the Higgs Boson H at the International Linear e^+e^- Collider
YUE Chong-Xing, FENG Hao-Lin, MA Wei

NUCLEAR PHYSICS

012101 Yrast Properties of Dysprosium Isotopes in the Double Mid-Shell Region
ZOU Wen-Hua, GU Jian-Zhong

012102 Nucleon-Nucleon Interaction and the Mixing of Scalar Meson
DAI Lian-Rong

012301 Search for Decay Rate Variation of ^{7}Be in Pt and Al
LI Cheng-Bo, ZHOU Shu-Hua, LIU Zhi-Yi, MENG Qiu-Ying, ZHOU Jing, LI Xiao-Mei, FU Yuan-Yong, WEN Qun-Gang, HU Shou-Yang

012401 A Microscopic Optical Potential for Deuteron
GUO Hai-Rui, HAN Yin-Lu, SHEN Qing-Biao

012501 Observation of Influence of Nucleons' Motion on Kaons Collective Flow in Dense Medium
XING Yong-Zhong, ZHENG Yu-Ming, WANG Yan-Yan, ZHANG Lin, QU Shi-Xian

ATOMIC AND MOLECULAR PHYSICS

013101 Excitation and Ionization of Ethylene by Charged Projectiles
WANG Zhi-Ping, WANG Jing, ZHANG Feng-Shou

013201 Dynamical Behavior of an Atomic Beam Interacting with a Fock State Light Field
LI Ben, CHEN Jing-Biao

013202 Measurement of Secular Motion Frequency in Miniature Paul Trap to Ascertain the Stability Parameters
GUO Bin, GUAN Hua, LIU Qu, HUANG Yao, HUANG Xue-Ren, GAO Ke-Lin

013301 Effect of Pressure on Absorption Spectra of Lycopene in n-Hexane and CS_2 Solvents
ZHANG Wei, LIU Wei-Long, ZHENG Zhi-Ren, HUO Ming-Ming, LI Ai-Hua, YANG Bin

013401 Positron-Impact Excitation of Hydrogen Atoms in Debye Plasmas
ZHANG Song-Bin, QI Yue-Ying, QU Yi-Zhi, CHEN Xiang-Jun, WANG Jian-Guo

FUNDAMENTAL AREAS OF PHENOMENOLOGY(INCLUDING APPLICATIONS)

014101 Method of Fundamental Solution for Composite Electromagnetic Scattering from Two-Dimensional Object Located on a Rough Surface
ZHANG Min, LUO Wei, LIU Jiang-Tao, BAI Lu, ZHOU Ping

014102 Left-Handed Effect of Composite Rectangular SRRs and Its Application in Patch Antennae
HUANG Ming, ZHOU Yue-Qun, SHEN Ting-Gen

014201 Non-Paraxial Split-Step Semi-Vectorial Finite-Difference Method for Three-Dimensional Wide-Angle Beam Propagation
CHENG Hua, ZANG Wei-Ping, ZHAO Zi-Yu, LI Zu-Bin, ZHOU Wen-Yuan, TIAN Jian-Guo

014202 Transverse Multimode Evolution in Non-Adiabatic Optical Micro/Nanofiber Tapers
FU Jian, XU Ying-Ying, TANG Shao-Fang, LI Yang, SUN Shuo

014203 Generation of High-Repetition-Rate Pulse Trains through the Continuous-Wave Perturbed by a Weak Gaussian Pulse in an Optical Fiber
ZHONG Xian-Qiong, XIANG An-Ping

014204 Highly Symmetric Planar Metamaterial Absorbers Based on Annular and Circular Patches
ZHU Wei-Ren, ZHAO Xiao-Peng, BAO Shi, ZHANG Yan-Ping

014205 Spatial Dispersion Induced by Cross-Phase Modulation
SHI Mei-Zhen, LI Chuang-She, ZUO Cui-Cui, ZHANG Yan-Peng, NIE Zhi-Qiang, ZHENG Huai-Bin, LI Chang-Biao, SONG Jian-Ping, GAN Chen-Li

014206 Period Continuous Tuning of an Efficient Mid-Infrared Optical Parametric Oscillator Based on a Fan-out Periodically Poled MgO-Doped Lithium Niobate
XIONG Bo, ZHANG Shu-Bao, GUO Lin, ZHANG Ling, LIN Xue-Chun, LI Jin-Min

014207 Efficient Long Wave IR Laser from Ho:YAG 2 μm Pumped $ZnGeP_2$ Optical Parametric Oscillator
LI-Gang, YAO Bao-Quan, DUAN Xiao-Ming, ZHU Guo-Li, WANG Yue-Zhu, JU You-Lun

014208 A Kind of Double-Cladding Photonic Crystal Fiber with High Birefringence and Two Zero-Dispersion Wavelengths
ZHOU Hong-Song, LI Shu-Guang, FU Bo, YAO Yan-Yan, ZHANG Lei

014209 Optical Switch Formation in Antimony Super-Resolution Mask Layers Induced by Picosecond Laser Pulses
ZHAI Feng-Xiao, ZUO Fang-Yuan, HUANG Huan, WANG Yang, LAI Tian-Shu, WU Yi-Qun, GAN Fu-Xi

014210 Fabrication of Optical Fiber Bragg Grating Assisted Mismatched Coupler
LIU Zhi-Ming, LI Jian, ZHENG Jing-Jing, FAN Lin-Yong, JIANG Wei-Wei, JIAN Shui-Sheng

014211 Experimental Properties of Optical Phase Conjugation in Cold Atoms in a Magneto-Optical Trap
ZHOU Shu-Yu, XIA Tian, XU Zhen, WANG Yu-Zhu

014212 Quantum Entropy Controlling in the Damping Jaynes–Cummings Model
JIA Fei, XIE Shuang-Yuan, YANG Ya-Ping

014213 Output Characteristics of an InP/InGaAsP Triangle Microcavity Laser
WANG Shi-Jiang, HUANG Yong-Zhen, YANG Yue-De, HU Yong-Hong, XIAO Jin-Long, DU Yun

014301 Vibration Characteristics of Acoustically Levitated Object with Rigid and Elastic Reflectors
HONG Zhen-Yu, XIE Wen-Jun, WEI Bing-Bo

014701 A Modified LBM Model for Simulating Gas Seepage in Fissured Coal Considering Klinkenberg Effects and Adsorbability-Desorbability
TAN Yun-Liang, TENG Gui-Rong, ZHANG Ze

014702 An Approximate Analytical Solution of Imploding Strong Shocks in a Non-Ideal Gas through Lie Group Analysis
L. P. Singh, Akmal Husain, M. Singh

CONDENSED MATTER: STRUCTURE, MECHANICAL AND THERMAL PROPERTIES

016101 Indication of Low-Energy BC_5 Structures
SHAO Xi

016201 Inhomogenous Dislocation Nucleation Based on Atom Potential in Hexagonal Noncentrosymmetric Crystal Sheet
ZHAO Xue-Chuan, LIU Xiao-Ming, ZHUANG Zhuo, LIU Zhan-Li, GAO Yuan

016202 Evaluation of Thermal Degradation Induced Material Damage Using Nonlinear Lamb Waves
XIANG Yan-Xun, XUAN Fu-Zhen, DENG Ming-Xi

016301 The Influence of Cap and Defect Layer on Interface Optical-Phonon Modes in Finite Superlattices
WANG Xin-Jun, LIU Jing-Feng, LUO Yong-Feng, LI Shui

016401 A Thermodynamic Cavitation Model for Cavitating Flow Simulation in a Wide Range of Water Temperatures
ZHANG Yao, LUO Xian-Wu, JI Bin, LIU Shu-Hong, WU Yu-Lin, XU Hong-Yuan

016402 Equation of State of Tantalum up to 133 GPa
TANG Ling-Yun, LIU Lei, LIU Jing, XIAO Wan-Sheng, LI Yan-Chun, LI Xiao-Dong, BI Yan

CONDENSED MATTER: ELECTRONIC STRUCTURE, ELECTRICAL, MAGNETIC, AND OPTICAL PROPERTIES

017101 First Principles Study of Adsorption and Reaction of CO on $SrTiO_3$ (100) Surface: the Role of Surface Oxygen Vacancies
YUN Jiang-Ni, ZHANG Zhi-Yong, YAN Jun-Feng, ZHANG Fu-Chun

017102 A First Principles Study on $m\mathrm{Al_{Zn}} - n\mathrm{N_O}$ Complex Doped ZnO
SHI Li-Bin, CHI Feng, XU Cui-Yan

017201 Influence of Rashba SOI and Polaronic Effects on the Ground-State Energy of Electrons in Semiconductor Quantum Rings
Eerdunchaolu, XIN Wei, ZHAO Yu-Wei

017301 Effect of Different Substrate Temperature on Sb-Doped ZnO Thin Films Prepared by Pulsed Laser Deposition on Sapphire Substrates
ZHAO Zi-Wen, HU Li-Zhong, ZHANG He-Qiu, SUN Jing-Chang, BIAN Ji-Ming, SUN Kai-Tong, CHEN Xi, ZHAO Jian-Ze, LI Xue, ZHU Jin-Xia

017302 Cap Layer Influence on Impurity-Free Vacancy Disordering of InGaAs/InP Quantum Well Structure
AN Yu-Peng, YANG Hua, MEI Ting, WANG Yi-Ding, TENG Jing-Hua, XU Cheng-Dong

017303 Fabrication and Characterization of C_{60}-Based Organic Schottky Diodes
CHENG Xiao-Man, HU Zi-Yang, WU Ren-Lei, WANG Zhong-Qiang, YIN Shou-Gen

017401 Electronic, Vibrational, and Superconducting Properties of High-Pressure Metallic SiH_4: *ab initio* Calculations
YAN Yan, GONG Jie, ZONG Zhan-Guo

017501 Effect of Sputtering Parameters on Film Composition, Crystal Structure, and Coercivity of SmCo Based Films Deposited on Si (100) Substrates
XUE Gang, PENG Long, ZHANG Huai-Wu

017502 Fabrication and Characterization of $Mn_{0.5}Zn_{0.5}Fe_2O_4$ Magnetic Nanofibers
XIANG Jun, SHEN Xiang-Qian, SONG Fu-Zhan, MENG Xian-Feng

017601 Electron Paramagnetic Resonance and Optical Absorption of VO^{2+} Doped Bis (glycinato) Mg (II) Monohydrate Single Crystals
Prashant Dwivedi, Ram Kripal, Santwana Shukla

017701 Phase Structures of $(K_{0.48}Na_{0.52})_{0.945}$ $Li_{0.055}Sb_{0.05}Nb_{0.95}O_3$ Piezoceramics
ZANG Guo-Zhong, YI Xiu-Jie, XU Zhi-Jun, FU Peng, ZHAO Li-Min, PU Xi-Peng

017702 Effects of Depolarization Field and Interfacial Coupling on the Polarization of Ferroelectric Bilayers
ZHENG Chao-Dan, ZHANG Duan-Ming, LIU Xin-Ming, YANG Bin, LIU Chao-Jun, YU Jun

017801 Beam Adjustment with Double Subwavelength Metal Slits Surrounded by Tapered Dielectric Gratings
ZOU Da-Qing, JIANG Jian-Li, LI Xiang-Yin

017802 Dielectric Properties of GaN in THz Frequencies
FANG He-Nan, ZHANG Rong, LIU Bin, LU Hai, DING Jian-Ping, XIE Zi-Li, XIU Xiang-Qian, ZHENG You-Dou, XIAO Ming-Wen, ZHANG Cai-Hong, CHEN Jian, WU Pei-Heng

CROSS-DISCIPLINARY PHYSICS AND RELATED AREAS OF SCIENCE AND TECHNOLOGY

018101 Giant Temperature Coefficient of Resistance in ZnO/Si (111) Thin Films
ZHOU Xiao-Fang, ZHANG Hui, LI Yong, TANG Xiao-Dong, CHEN Qing-Ming, ZHANG Peng-Xiang

018102 Preparation and Characteristics of GaN Films on Freestanding CVD Thick Diamond Films
ZHANG Dong, BAI Yi-Zhen, QIN Fu-Wen, BIAN Ji-Ming, JIA Fu-Chao, WU Zhan-Ling, ZHAO Ji-Jun, JIANG Xin

018301 Rheological Behavior of Some Aqueous Gels of Carbopol with Pharmaceutical Applications
M. Todica, C. V. Pop, L. Udrescu, M. Pop

018501 Optical Switching of a Quantum Cascade Laser in Continuous Wave Operation
Gang Chen, Seong-wook Park, I-Chun A. Chen, Clyde G. Bethea, Rainer Martini

018502 Evaluating of Adhesion Property of ULSI Interconnect Films by the Surface Acoustic Waves
XIAO Xia, SHAN Xing-Meng, LIU Ya-Liang

018503 Nonvolatile Memory Effect in Organic Thin-Film Transistor Based on Aluminum Nanoparticle Floating Gate
WANG Wei, MA Dong-Ge

018701 Competitive Exclusion Principle Revised by Noise
LIU Yong-Jiang, WANG Ai-Ling, WANG Biao, LIU Zhao-Hua

018702 Application of Small-World Measures to Multichannel Event-Related Potential Activity during Generation of Global and Local Imagery
SUI Dan-Ni, ZHAO Qing-Bai, TANG Yi-Yuan

GEOPHYSICS, ASTRONOMY, AND ASTROPHYSICS

019401 Cluster Observation of Eelectrostatic Solitary Waves around Magnetic Null Point in Thin Current Sheet
LI Shi-You, DENG Xiao-Hua, ZHOU Meng, YUAN Zhi-Gang, WANG Jing-Fang, LIN Xi, LIN Min-Hui, FU Song

019601 Ion Velocity Distributions in a Non-Stationary Perpendicular Shock
YANG Zhong-Wei, LU Quan-Ming, WANG Shui